ACS APPLIED MATERIALS & INTERFACES

Research Article

www.acsami.org

Diamond Nanoparticles as a Support for Pt and PtRu Catalysts for Direct Methanol Fuel Cells

Lyda La-Torre-Riveros,[†] Rolando Guzman-Blas,[†] Adrián E. Méndez-Torres,[‡] Mark Prelas,[‡] Donald A. Tryk,[†] and Carlos R Cabrera*[,†]

[†]NASA-URC Center for Advanced Nanoscale Materials, Department of Chemistry, University of Puerto Rico, Río Piedras, P.O. Box 70377, San Juan, Puerto Rico 00936-8377

[‡]Nuclear Science and Engineering Institute, E2433 Engineering Building East, University of Missouri, Columbia, Missouri 65211, United States

Supporting Information

ABSTRACT: Diamond in nanoparticle form is a promising material that can be used as a robust and chemically stable catalyst support in fuel cells. It has been studied and characterized physically and electrochemically, in its thin film and powder forms, as reported in the literature. In the present work, the electrochemical properties of undoped and boron-doped diamond nanoparticle electrodes, fabricated using the ink-paste method, were investigated. Methanol oxidation experiments were carried out in both half-cell and full fuel cell modes. Platinum and ruthenium nanoparticles were chemically deposited on undoped and boron doped diamond nanoparticles through the use of $NaBH_4$ as reducing agent and sodium dodecyl benzene sulfonate (SDBS) as a surfactant. Before and after the reduction process, samples were characterized by electron microscopy and spectroscopic techniques. The ink-paste method was also used to prepare the membrane electrode assembly with Pt and Pt−Ru modified undoped and boron-doped diamond nanoparticle catalytic systems, to perform the electrochemical experiments in a direct methanol fuel cell system. The results obtained demonstrate that diamond supported catalyst nanomaterials are promising for methanol fuel cells.

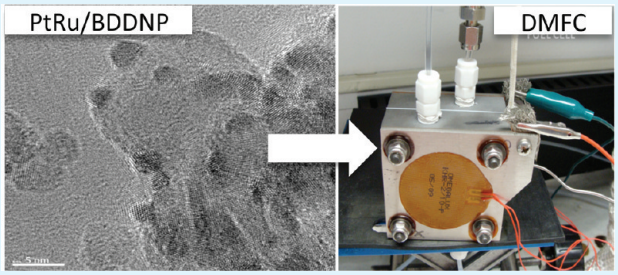

KEYWORDS: *diamond nanoparticles, Pt−Ru catalyst, membrane electrode assembly, fuel cell, methanol oxidation*

1. INTRODUCTION

Recent intensified research efforts in the low temperature fuel cell area have focused on catalyst development in order to significantly decrease costs and improve durability.[1] Specifically, noble metal loadings must be drastically decreased to levels well below 1.0 mg cm^{-2}. Highly dispersed catalysts on carbon blacks have been developed and are widely used but suffer from poor durability, particularly under start−stop conditions and fuel starvation conditions, during which high potentials can be reached.[2−6]

One of the most promising alternative support materials that has been considered is diamond, because of its extreme chemical and electrochemical stability, although in its non-doped form, it has insufficient electrical conductivity.[7,8] Diamond in nanoparticle form affords the opportunity of more facile doping due to its high surface area.[9,10] If convenient ways to dope diamond nanoparticles could be developed, the latter could be quite promising as an electrocatalyst support material.[11,12]

A common route to prepare nanoparticle diamond is via detonation, which produces particles in the 2−10 nm range. However, much graphitic material is alsoproduced and must be removed in order for the high stability of the diamond to be exhibited. Both air oxidation[13] and aqueous acidic treatment[14,15] have been used as purification methods. Even after extensive purification, there can remain sufficient graphitic material and thus electronic conductivity for use as analytical electrodes in the form of cast films or mineral oil pastes.[16,17,12]

There are different methods to dope diamond films, such as ion infiltration and ion implantation.[18] However, there have been few attempts to dope diamond nanoparticles. Prelas et al.[19] reported the electric field-enhanced diffusion (EFED) method as a successful method to dope diamond films, and field-enhanced diffusion with optical activation (FEDOA)[20] for microsized diamond was also tested for diamond nanoparticles. The ion implantation method makes use of high energy ions, which introduce damage into the crystal structure, which must be removed by annealing. In contrast, the EFED and FEDOA methods do not damage the crystal structure of the material. The conditions used in the latter two methods are high temperatures, time control, strong electric field, and optical ionization (laser illumination).

Received: January 16, 2012
Accepted: January 23, 2012
Published: January 23, 2012

Various methods have been developed for the preparation of Pt and PtRu electrocatalysts including impregnation,[21,22] microemulsion,[23,24] and colloidal routes.[25−27] Problems with the control of particle size and distribution have been reported,[21,22] which have been somewhat alleviated by use of surface treatments.[28] Chemical reduction with agents such as $NaBH_4$,[28] KBH_4,[29] H_2O_2,[30] hydrazine hydrate ($N_2H_4{\cdot}H_2O$),[31] and plasma reduction[32] have been used to deposit these metals on carbon, as well as on DNP surfaces.[33] As we show in the present work, one promising application for these catalytic systems is the direct methanol fuel cell (DMFC), which is one of the most attractive systems studied in the electrochemical energy conversion field.[34,35]

The DMFC differs from the polymer electrolyte membrane fuel cells (PEMFC) in the type of fuel used (liquid methanol vs hydrogen gas). DMFCs operate at higher temperatures (50−120 °C) and can reach 40% efficiency. The DMFC offers advantages compared to the PEMFC, such as the handling and storage of liquid methanol compared to that for hydrogen gas. However, DMFCs show lower power densities than PEMFCs owing to the slow methanol oxidation kinetics and other problems (e.g., methanol crossover through the membrane).[36] The most efficient methanol anodes are based on platinum and ruthenium. During methanol oxidation, pure platinum is poisoned by the adsorption of CO as an intermediate. The addition of ruthenium to platinum improves the rate of methanol oxidation via the bifunctional mechanism.[37] Measurements at Pt−Ru alloy electrodes of well characterized surface composition show that the activity for methanol oxidation at room temperature is high for low ruthenium coverage.[37]

In the present study, we report the development of dimensionally stable, high surface area diamond nanoparticles with high loadings of Pt and PtRu nanoparticles of small size, in the range of 2−5 nm, through a simple chemical reduction route using sodium borohydride and sodium dodecyl benzene sulfonate (SDBS) as a surfactant.[33] Both, the undoped and boron doped diamond particulates were pretreated with strong acid to improve the interaction of the metal ions with the surface. Electrochemical characterization was carried out by use of a three-electrode electrochemical cell, and performance tests were carried out in a methanol fuel cell at various temperatures in a single fuel cell station, in the half-cell and full-cell modes. These results demonstrate the efficacy of undoped DNPs and BDDNPs as catalyst supports for DMFCs.

2. EXPERIMENTAL SECTION

Previously purified samples of undoped DNPs and BDDNPs[14,15] were used to perform electrochemical experiments and chemical depositions of metallic catalysts. BDDNPs were obtained by the field-enhanced diffusion optical activation (FEDOA) technique; they were cleaned by refluxing with nitric acid, as were the undoped DNPs. In the FEDOA method, 1 g of undoped, purified diamond nanoparticles was mixed with three times this amount of boron powder and subjected to a forced diffusion process. In this process, a temperature range of 750 − 950 °C, a potential difference of 150 V, a pressure of 20 − 40 mmHg and a laser source were employed in the optimized experimental conditions to obtain the BDDNPs.[20b] Physicochemical and spectroscopic characterization results of unpurified and purified samples are reported in our previous work.[15,38]

2.1.1. Cyclic Voltammetry (CV). *Preparation of the Working Electrode.* To prepare the working electrode, a 1 mg sample of purified nanoparticles to be studied was mixed with Nafion (5 μL, 5 vol%) and isopropyl alcohol (250 μL) (ink-paste method). The suspension obtained was sonicated for 5 h. Twelve microliters of suspension was pipetted out and delivered onto a glassy carbon surface. After the electrode coating was dried in air at room temperature, it was submerged in an electrochemical cell containing 0.5 M H_2SO_4 solution as the electrolyte. The amounts used to prepare the ink-paste were determined by doing several experiments in the electrochemical cell, varying the volumes of Nafion solution, and isopropyl alcohol, and the sample mass. An Ag/AgCl reference electrode and a graphite rod counter electrode were used. An AUTOLAB potentiostat was used in all electrochemical measurements. For Pt/DNP, Pt−Ru/DNP, Pt/BDDNP, and Pt−Ru/BDDNP catalytic systems, the same ink−paste method was used. After the electrode was prepared, it was submerged in an electrochemical cell. The chemically reduced samples were studied with cyclic voltammetry in 0.5 M H_2SO_4, and CO stripping experiments. These experiments were carried out to calculate the electrochemically active surface area of Pt.

For the CO stripping experiments, 0.5 M H_2SO_4 solution was purged with CO and a potential of 0.1 V vs Ag/AgCl was applied to the electrode for 15 min. After this, CO was changed to N_2 gas and the solution was purged for 10 min to remove free CO molecules from the solution. For methanol oxidation on Pt/DNP, Pt−Ru/DNP, Pt/BDDNP, and Pt−Ru/BDDNP catalytic systems, the chemically reduced samples obtained were tested in an electrochemical cell containing a 1 M methanol solution in 0.5 M H_2SO_4.

2.2. Chemical Deposition of Pt and Pt−Ru Catalysts on Undoped Diamond Nanoparticles and Boron-Doped Diamond Nanoparticles Using a Mild Reducing Agent and a Surfactant. The DNP and BDDNP surfaces were decorated with platinum and ruthenium nanoparticles produced through the reaction of a 5-fold excess of sodium borohydride (Aldrich, 99%) as a reducing agent, and $H_2PtCl_6{\cdot}xH_2O$ (Aldrich, 99.995%), and $RuCl_3{\cdot}xH_2O$ (Alfa Aesar, 99.99%) as the platinum and ruthenium sources. Suspensions of the DNPs and the platinum salt solutions in the appropriate concentration to produce 50 wt % of metallic platinum or the desired amount (see Table 1) of platinum and ruthenium were prepared. To ensure intimate contact between the diamond nanoparticles and the metal ion-containing solutions, the suspensions were sonicated for a period of 5−8 h. After the sonication process, the reducing agent was directly added. The last step was carried out under vigorous stirring until the reaction was completed. Finally, the sample was filtered by washing with copious amounts of nanopure water to eliminate the ions produced in the reaction, dried for 15 min at 115 °C in air, and stored in a desiccator. Additional samples of undoped DNP and BDDNP were decorated with platinum and ruthenium nanoparticles produced through the reaction of excess sodium borohydride plus sodium

Table 1. Expected Amounts of Pt and Ru at DNP and BDDNP Samples under Study Using Five-Fold Excess $NaBH_4$ Reducing Agent

	sample	catalyst (% wt)	reducing agent ($NaBH_4$ × 5)	surfactant (SDBS)
1	DNP (purified HNO_3 c)	Pt (50)	+	
2	DNP (purified HNO_3 c)	Pt−Ru (40−15)	+	
3	BDDNP (cleaned HNO_3 diluted)	Pt (50)	+	
4	BDDNP (cleaned HNO_3 diluted)	Pt−Ru (40−15)	+	
5	DNP (purified HNO_3 c)	Pt (50)	+	+
6	DNP (purified HNO_3 c)	Pt−Ru (40−15)	+	+
7	BDDNP (cleaned HNO_3 diluted)	Pt (50)	+	+
8	BDDNP (cleaned HNO_3 diluted)	Pt−Ru (40−15)	+	+

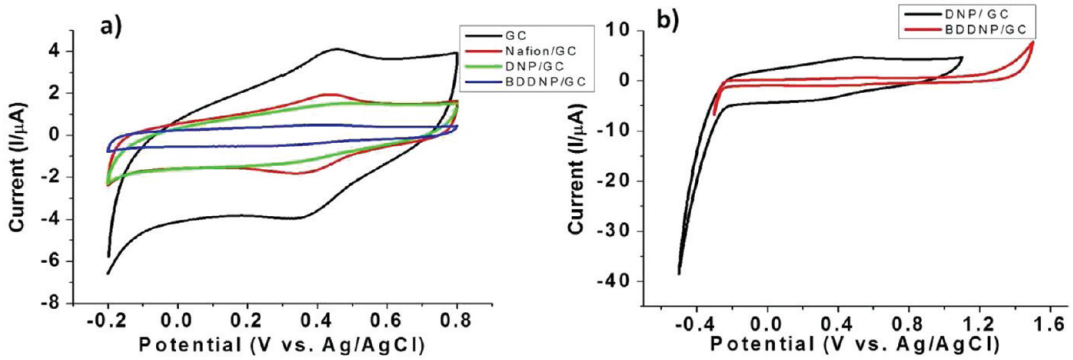

Figure 1. Cyclic voltammograms of: (a) glassy carbon (GC) (black line), Nafion on GC (red line), purified undoped DNPs (green line), purified BDDNPs (blue line); (b) purified undoped DNPs (black line), purified BDDNPs (red line) in 0.5 M H_2SO_4 aqueous solution as supporting electrolyte.

dodecyl benzene sulfonate (SDBS, 0.14 M).[28,39] Again, suspensions were prepared with platinum ion solution and the diamond nanoparticles, in an appropriate concentration in order to produce 50 wt % of metallic platinum or the desired amount of platinum and/or ruthenium. The suspensions were also sonicated for 5 h. During this process, the platinum ions were surrounded by SDBS ions until the reducing agent was added. These ions encapsulate the metal ions and thus help to obtain small, well-dispersed nanoparticles. Prior to the addition of the reducing agent, 1 M NaOH solution was added in an amount sufficient to reach a pH of 9; the solution was then stirred for 2 h to release the SDBS ions from the metal ions. After this process, a 5-fold excess of the reducing agent was directly added, and the same procedure was followed as used for the samples synthesized without SDBS.

2.3. Single Methanol Fuel Cell Assembly. In this section, a detailed description of the single fuel cell assembly and performance is presented. The membrane-electrode assembly (MEA) consisted of seven layers: a proton exchange membrane, anode and cathode catalyst layers, two gas diffusion layers (GDLs), and two sets of sealing gaskets. The current collectors or GDLs were made of electrically conductive materials such as carbon paper and carbon cloth; these were modified with the catalyst ink by the GDL-based method, where the catalyst ink was painted on the GDL and hot-pressed on the membrane. After the MEAs were prepared, they were assembled in a single fuel cell system to carry out anodic polarization measurements, with a hydrogen-fed counter electrode. Finally, the full cell characteristics were measured with an air-fed cathode, and the power produced from the fuel cell was determined to define its efficiency.[40]

2.3.1. Catalyst Ink Preparation. The catalyst ink was made using a general method used in MEA fabrication,[40,41] which consists of mixing appropriate amounts of diamond-supported catalyst with Nafion (5% in isopropyl alcohol, Aldrich), nanopure water and in this case, isopropyl alcohol (Aldrich) and methanol as solvents. The diamond-supported catalyst was placed in an ultrasonic bath with the solvents for 6−8 h, followed by stirring for 24 h to disperse the nanoparticle clusters as much as possible. In the case of the ink prepared for the cathode, platinum black, nanopure water, Nafion, methanol, and isopropyl alcohol were thoroughly mixed and a Teflon (12 vol%) suspension was also used. The catalyst samples used for the MEA fabrication are mentioned in Table 1.

The loadings are given in terms of mg of metal per cm^2 (geometric area of the diffusion layer 5 cm^2). For all synthesized diamond supported catalysts for the anode, the metal loading was approximately 4 mg cm^{-2}; this loading was also used for the cathode.[40]

2.3.2. Anode and Cathode Fabrication. Anode fabrication starts in a blocking process of the carbon paper surface (5 cm^2) with a Vulcan carbon ink, which was prepared using nanopure water, methanol, isopropyl alcohol, and Nafion. After several layers of the ink were deposited, the electrode was dried, weighed and painted until a mass of approximately 1 mg cm^{-2} was reached. Finally, the electrodes were numbered and stored in a desiccator. The blocked electrodes were painted with the corresponding ink of diamond-supported metal catalyst until the loading of 4 mg cm^{-2} Pt was reached.

Cathode fabrication was carried out by directly painting the platinum black catalyst ink on the carbon cloth, which had previously been blocked with carbon. The resulting cathodes were stored in a desiccator.

2.3.3. Fuel Cell Assembly. The assembly of a single fuel cell starts by arranging the membrane electrode assembly (MEA), placing the cathode on the center of one side of the Nafion membrane (N117), which was previously cleaned by boiling in a nitric acid solution (1:1) for 20 min, followed by another boiling process in nanopure water for 1 h. Both cathode and Nafion membrane were hot-pressed.

After the MEA was arranged, it was placed inside the single fuel cell system, and hydrated; this was done with a nanopure water flow overnight. The fuel cell was connected to a computer-controlled potentiostat (HCP-803) and to flow and temperature controllers. The flow controller was connected to H_2, N_2, air, or O_2 gas tanks and a liquid absorber with a filter used for water or methanol feed. The hydrating process is necessary to stabilize the electrolyte membrane (Nafion) of the MEA. After hydrating overnight with a flow of 2 mL min^{-1}, the working temperature was set.

For anodic polarization, the assembled single fuel cell was connected to the potentiostat (HCP-803) through the corresponding anode and cathode connections. The temperature was set at 25 °C, nitrogen gas was flowed (120 mL min^{-1}) through the cathode and nanopure water (2 mL min^{-1}) through the anode for 15 min. Then pure water was replaced with an aqueous 1 M methanol solution. After 15 min, this was replaced with hydrogen gas. The anode must show a low (close to 0.0 V vs Pt/H_2) potential value to start the anodic linear polarization. For the anodic polarization, a potential range from 0.0 to 0.5 V, at a scan rate of 0.5 mV s^{-1} was applied and a potential − current plot was obtained. Immediately after the anodic polarization, linear polarization of the cell was performed, in which the fuel cell was cleaned with a flow of nanopure water at the anode and nitrogen gas at the cathode for 2 h. After cleaning the cell, water flow was changed to 1 M methanol in water solution and nitrogen was replaced with air at a temperature of 25 °C, and a potential range from 0.0 to 0.404 V, at a scan rate of 0.5 mV s^{-1} was applied and a potential−current plot was obtained. In all cases, current responses were normalized to the electrode surface area of 5 cm^2.

These procedures were carried out with all eight samples at 25, 60, and 80 °C, and repeated 3 times for reproducibility, to observe the temperature effect on the catalyst performance.

2.4. Physicochemical, Spectroscopic and Electrochemical Characterization of Catalyst Systems (Pt, PtRu on DNPs and BDDNPs). The metal concentrations in the samples and the reagents used for synthesis of the nanoparticles are presented in Table 1.

In X-ray diffraction characterization, a SIEMENS D5000 X- ray diffractometer with Cu Kα radiation and a Rigaku Ultima III X-ray diffractometer with Cu Kα radiation were used. All samples studied, including undoped DNPs, BDDNPs and supported Pt and Pt−Ru

Table 2. Functional Groups and X-ray Photoelectron Spectroscopy Counts and Binding Energy Peaks Obtained from Pt and Pt−Ru on Undoped DNPs and BDDNPs

	C_{1s} a.u.				O_{1s} a.u.		Pt a.u.		Ru a.u.	
sample	C	−CO	−COOH	CO+COOH/C	−COH	−OH	$Pt_{4f\ 7/2}$, 71−72 eV	$Pt_{4f\ 5/2}$, 74−75 eV	3_p ∼462 eV	water ligand ∼466 eV
1	2200	399	160	0.25	110	580	1970	1280		
2	1000	720	1320	2.04	620	1260	1020	800	305	90
3	4400	900		0.20	3000	7200	5800	3600		
4	4900	2100	580	0.55	3500	5100	7900	4480	1320	210
5	14000	1900		0.14	600	3900	4400	2840		
6	12950	1000		0.08	900	3550	3490	2400	670	170

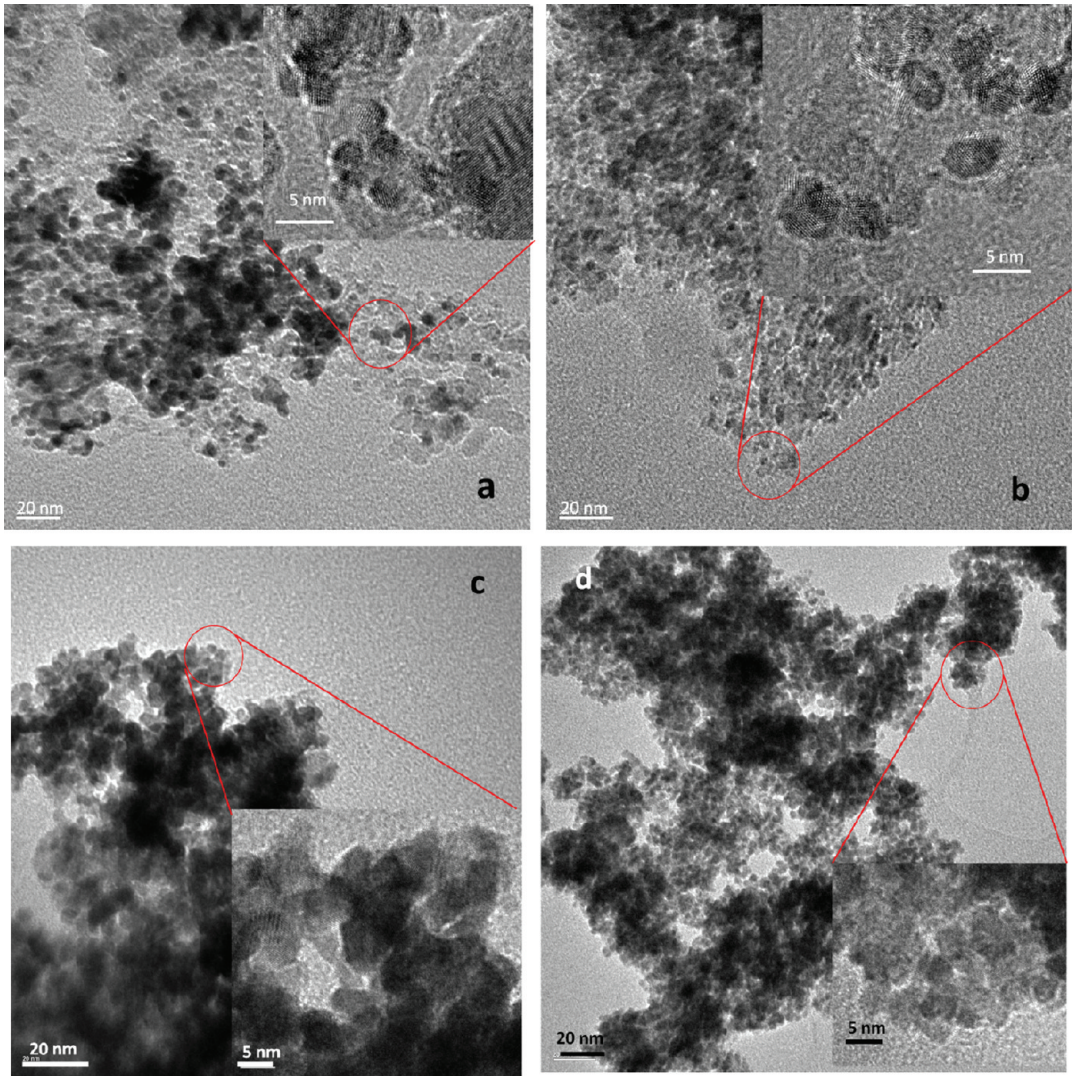

Figure 2. Transmission electron micrographs of: (a) Pt/undoped DNPs, (b) Pt−Ru/undoped DNPs, (c) Pt/BDDNPs, and (d) Pt−Ru/BDDNPs, bar scales 20 and 5 nm; samples obtained by use of excess $NaBH_4$.

catalyst systems, were analyzed by the use of X-ray photoelectron spectroscopy with a PHI 5600 spectrometer. A boron-doped diamond sample was cleaned in a reflux system with concentrated nitric acid to eliminate the excess boron present in the sample. For the transmission electron microscopy, Carl Zeiss 200-kV and Gatan TG120 transmission electron microscopes were used to obtain the micrographs shown below.

2.5.1. Results. *Cyclic Voltammetry of Undoped DNPs and BDDNPs.* Samples of undoped and boron-doped diamond nanoparticles purified in concentrated HNO_3 were investigated to observe their electrochemical behavior in 0.5 M H_2SO_4. Figure 1a shows a comparison of the electrochemical response among bare glassy carbon, Nafion (5 μL Nafion in 250 μL of isopropanol) on glassy carbon, DNP ink-paste on glassy carbon and BDDNP ink-paste on glassy carbon (GC) using 0.5 M H_2SO_4 as the electrolyte. There are noteworthy differences in the capacitances of all electrodes, going from the GC electrode (high capacitance) to BDDNP (lower capacitance); the potential range applied was 0.8 to −0.2 V (initial potential, 0.3 V) at 20 mV s^{-1}. Figure 1b shows the cyclic voltammetry of DNP and BDDNP electrodes over a broad range of potential, from 1.5 to −0.5 V at 20 mV s^{-1}, showing the hydrogen evolution and oxide formation at negative and positive potentials respectively which indicates the working voltage

dx.doi.org/10.1021/am2018628 | ACS Appl. Mater. Interfaces 2012, 4, 1134−1147

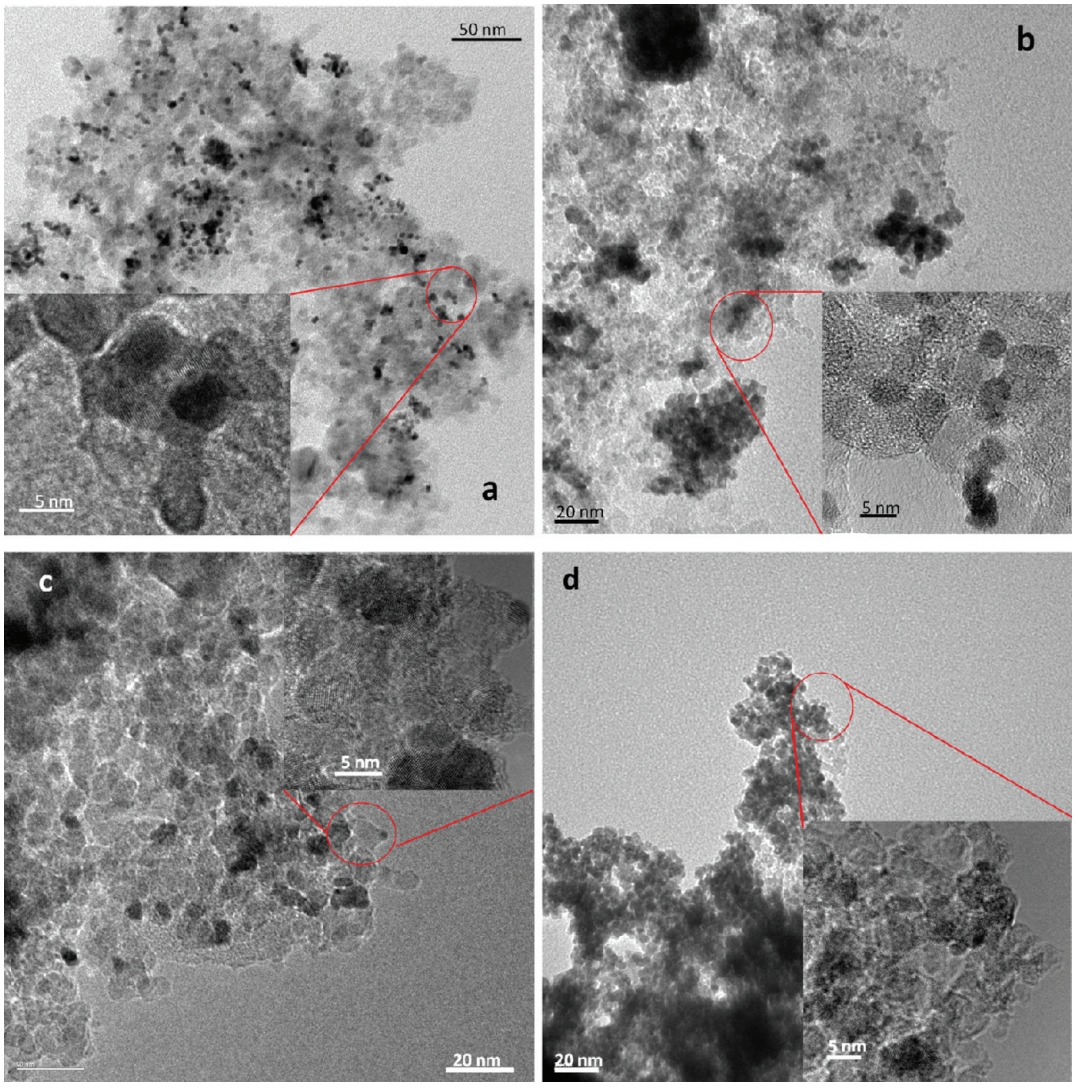

Figure 3. Transmission electron micrographs of: (a) Pt/DNPs, (b) Pt−Ru/DNPs, (c) Pt/BDDNPs, and (d) Pt−Ru/BDDNPs obtained use of excess $NaBH_4$ and SDBS.

limits of the electrodes. Cyclic voltammograms of redox couples at the diamond surface are included in the Supporting Information.

2.5.2. X-ray Diffraction (XRD). X-ray diffraction characterization was carried out to indicate the presence of platinum and ruthenium-modified platinum on the diamond nanoparticle surfaces. Representative diffractograms are shown in the Supporting Information, and XRD patterns for samples synthesized using SDBS are also included. The results confirm that the Pt and Pt−Ru catalysts present XRD characteristics similar to those found in the literature for such catalysts supported on carbon blacks.[42] For example, evidence was found for Pt−Ru interactions, indicative of alloying, as discussed latter.

2.5.3. X-ray Photoelectron Spectroscopy (XPS). High-resolution X-ray photoelectron spectroscopy (XPS) spectra of C 1s, O 1s, and B 1s binding energy regions for DNPs, and BDDNPs, were recorded and are reported in our previous work for similar samples with lower metal loadings.[33] In the present work, the XPS results for higher metal loadings prepared using a 5-fold excess of $NaBH_4$ (see the Supporting Information) were very consistent with the previous ones. The carbon region shows the presence of carbonyl (−C═O) and carboxylic groups. The oxygen region shows alcohol (−C−OH) and hydroxyl (OH^-) groups, and the B 1s region shows signals from elemental boron (190.5 eV), and B_2O_3 (193 eV).[43] The amount of boron present in the purified sample was determined by XPS using the area percentages of boron and carbon, resulting in a concentration of 0.68 at%. Furthermore, the B 1s peak was broad, evidence for the interaction of boron with the diamond matrix.

The XPS spectra of undoped DNPs with deposited Pt and Pt−Ru nanoparticles exhibited C 1s, O 1s, P 4f, and Ru 3p signals; these regions are described in Table 2. For these four samples it is evident that platinum and platinum − ruthenium deposition occurs preferentially via the interaction with −OH groups on the diamond surfaces.

2.5.4. Transmission Electron Microscopy (TEM). TEM micrographs for the samples obtained using a 5-fold excess of reducing agent and a high percentage of platinum are presented in Figure 2 (a, b, c, d). A sample of undoped DNPs decorated with metallic Pt nanoparticles (50 wt % Pt, sample 1 in Table 1) is shown in Figure 2a. The platinum nanoparticles are approximately 2 − 3 nm in diameter and show a very well-defined crystal structure with lattice fringes for the atomic planes visible. Pt−Ru (40 wt % Pt−15 wt % Ru, sample 2 in Table 1) on undoped DNPs are shown in Figure 4b, where the metallic nanoparticles are also well dispersed. The bimetallic nanoparticles are 2−4 nm in diameter, and a well-defined crystal structure with corresponding lattice fringes, were also evident.

Platinum nanoparticles chemically deposited on the BDDNP surface are shown in Figure 2c, where it can be seen that metallic nanoparticles are covering almost the whole BDDNP surface, and some agglomeration is also evident. These metallic Pt nanoparticles were 4−5 nm; they also exhibited well-ordered atomic planes. Figure

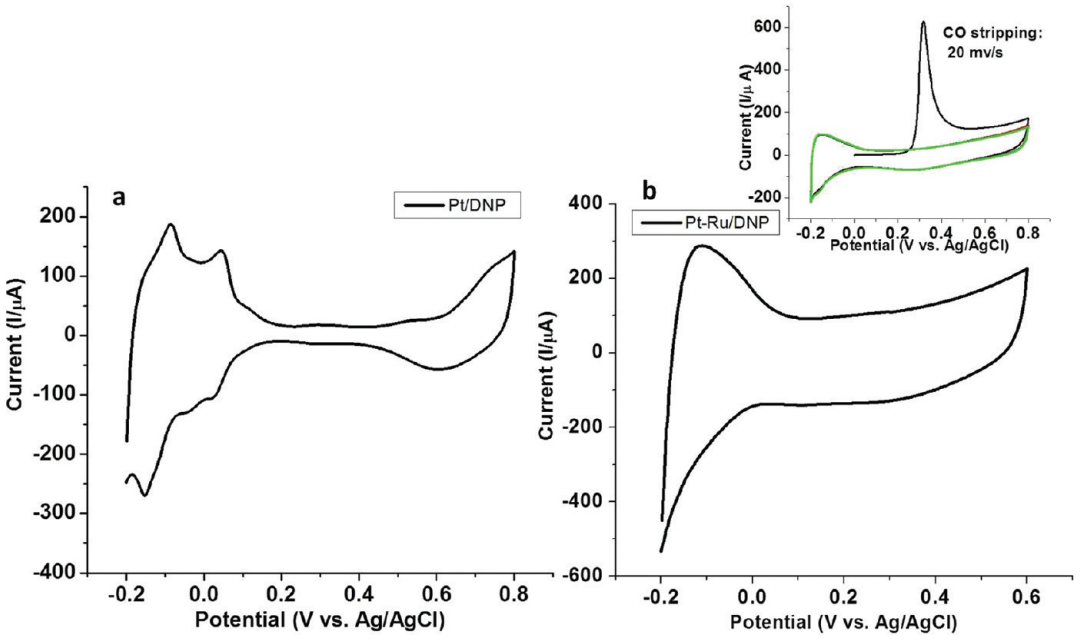

Figure 4. Cyclic voltammograms in H_2SO_4 0.5 M of (a) Pt/DNPs, and (b) Pt−Ru/DNPs (inset CO stripping), corresponding to samples 1 and 2 in Table 1.

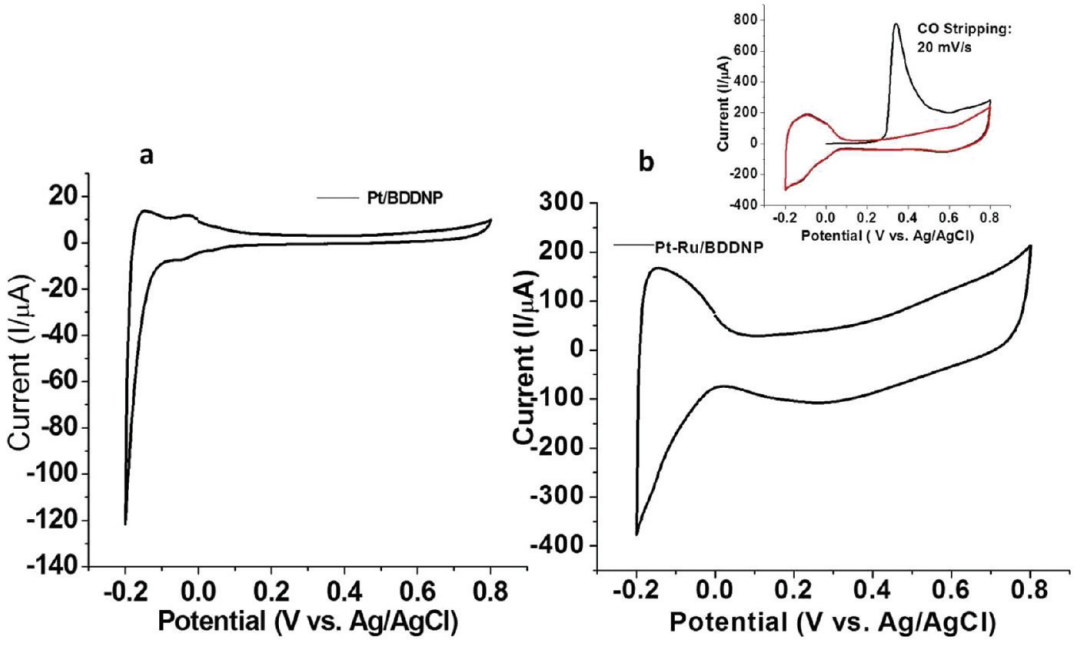

Figure 5. Cyclic voltammograms in H_2SO_4 0.5 M of (a) Pt/BDDNPs, and (b) Pt−Ru/BDDNPs, (inset CO stripping), corresponding to samples 3 and 4 in Table 1.

2d shows bimetallic Pt−Ru nanoparticles on BDDNP; their sizes were 4−5 nm, and agglomeration was also present; however, the atomic planes are clearly observed. For the catalyst systems obtained by use of SDBS, Figure 3a shows the TEM micrograph of metallic Pt nanoparticles chemically deposited on DNP surfaces purified in concentrated HNO_3 (50 wt % Pt) at different magnifications. The images clearly show very well dispersed dark Pt nanoparticles on the DNP surfaces. The Pt nanoparticles in this sample were around 3−4 nm, and the diamond nanoparticles were found to be 5−6 nm. Ru was also chemically reduced together with Pt on the surfaces of the DNP (40 wt % Pt−15 wt % Ru). Figure 3b shows images of bimetallic Pt−Ru nanoparticles (2−4 nm), and diamond nanoparticles (6−7 nm). Figure 3c shows dispersed Pt nanoparticles (2−5 nm) on BDDNPs (50 wt % Pt) and BDDNPs (5−6 nm). Chemical reduction of Pt and Ru metals was also performed on BDDNPs (40 wt % Pt−15 wt % Ru), Figure 3d shows the atomic planes of the bimetallic nanoparticles. The sizes of these bimetallic crystals were 2−4 nm. In all samples, the crystal facets of the metallic nanoparticles are visible, which indicates that the reduction in the presence of surfactant does not affect the crystal morphology but indeed helps to produce small, and in some cases, better dispersed nanoparticles.

2.5.5. Cyclic Voltammetry of Pt/DNP, Pt−Ru/DNP, Pt/BDDNP, and Pt−Ru/BDDNP Catalytic Systems. Cyclic voltammetry in 0.5 M H_2SO_4 (Figure 4) shows the characteristic peaks for hydrogen adsorption (negative current in the −0.2 to 0.1 V vs Ag/AgCl region) and desorption (positive current in the same potential region) of hydrogen on the nanocrystalline Pt surface. A cyclic voltammogram

dx.doi.org/10.1021/am2018628 | ACS Appl. Mater. Interfaces 2012, 4, 1134−1147

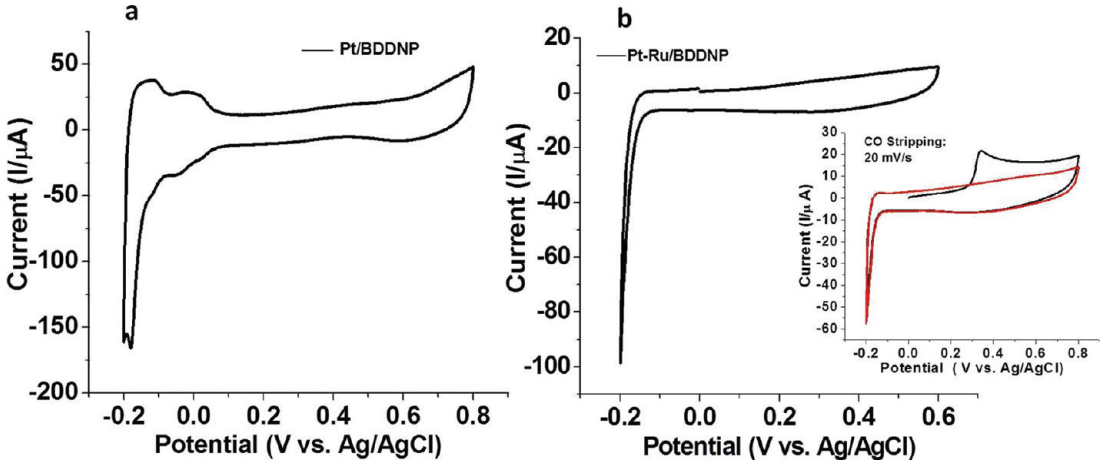

Figure 6. Cyclic voltammograms of (a) Pt/BDDNPs in H_2SO_4 0.5 M, and (b) Pt−Ru/BDDNPs in (a) H_2SO_4 0.5 M, and (inset) CO stripping experiment. Samples 7 and 8 in Table 1.

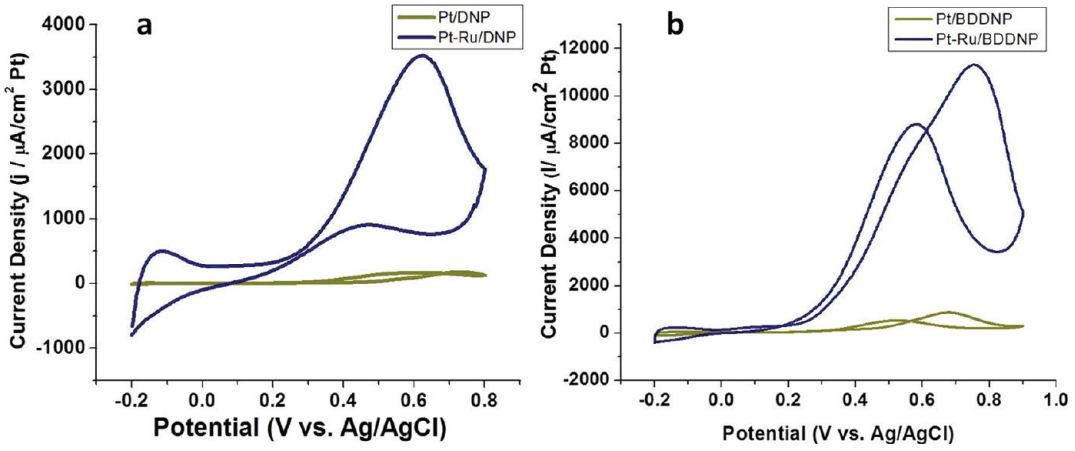

Figure 7. Cyclic voltammetry in 1 M methanol in H_2SO_4 0.5 M solution of: (a) Pt/DNPs, Pt−Ru/DNPs, and (b) Pt/BDDNPs, Pt−Ru/BDDNPs, corresponding to samples 1−4 in Table 1.

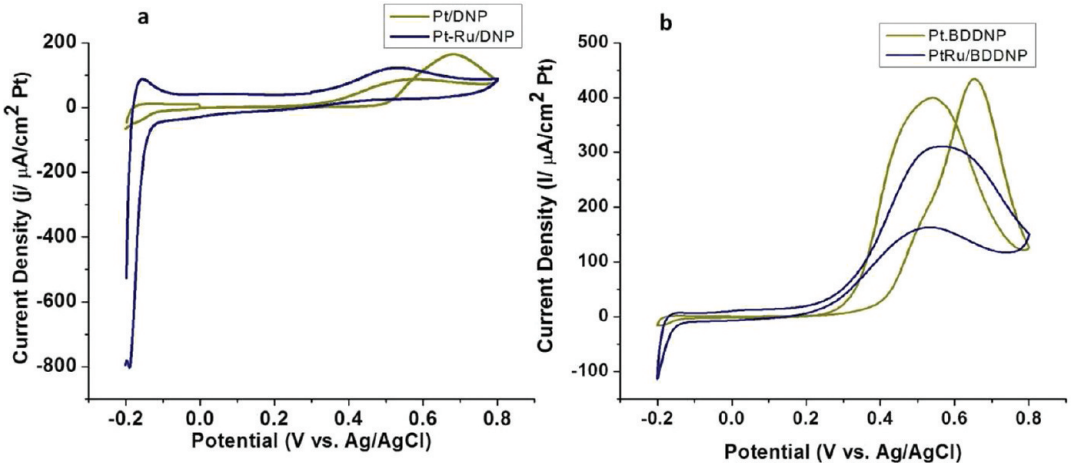

Figure 8. Cyclic voltammetry in 1 M methanol in H_2SO_4 0.5 M solution of: (a) Pt/DNPs, Pt−Ru/DNPs, and(b) Pt/BDDNPs, Pt−Ru/BDDNPs, corresponding to samples 5−8 in Table 1.

was obtained from 0.0 to 0.8 to −0.2 V at 20 mV s^{-1} to observe the CO oxidative desorption. A second voltammogram shows that all CO was desorbed from the Pt surface. Figure 4 (a, b) shows the cyclic voltammograms for Pt on undoped DNPs (samples 1 and 2 in Table 1) in 0.5 M H_2SO_4 with hydrogen adsorption and desorption on Pt, and it also shows voltammograms obtained from CO stripping (sample 2 of Table 1, Figure 4 b inset). A broad peak for CO desorption was observed at ca. 0.35 V for samples containing Pt−Ru nanoparticles. The same experiments were repeated and performed under the same conditions with samples 3, 4, 5, 6, 7, and 8 of Table 1. Some results of these experiments are shown in Figure 5a, b for samples 3 and 4. Figure 6a, b shows the cyclic voltammograms of Pt

dx.doi.org/10.1021/am2018628 | ACS Appl. Mater. Interfaces 2012, 4, 1134−1147

on BDDNPs (50 wt % Pt/DNPs using SDBS) in 0.5 M H_2SO_4, which shows hydrogen adsorption and desorption peaks on Pt, and it also shows CO stripping voltammograms obtained for the Pt–Ru/BDDNP catalyst system, where a broad peak at 0.38 V is observed. To calculate the Pt surface area from the voltammograms obtained in 0.5 M H_2SO_4, we used a charge of 210 μC cm^{-2} platinum and, in the case of CO stripping, a charge of 420 μC cm^{-2}.[44]

2.5.6. Methanol Oxidation on Pt/DNP, Pt–Ru/DNP, Pt/BDDNP, and Pt–Ru/BDDNP Catalytic Systems. In Figure 7a, b, the cyclic voltammetry in methanol solution of the Pt/DNPs catalyst shows characteristic peaks of catalyzed methanol oxidation in both sweep directions of the voltammogram, showing a maximum current density of ca. 220 μA cm^{-2} Pt. Similar behavior was observed with Pt–Ru/DNPs but with a greatly increased maximum current density (ca. 4500 μA cm^{-2} Pt). The catalytic behavior of the Pt/BDDNPs sample was also characteristic for methanol oxidation, reaching a maximum value of ca. 880 μA cm^{-2} Pt. Again, a greatly increased maximum current density (ca. 11000 μA cm^{-2} Pt) was observed for Pt–Ru/BDDNPs. Both of the latter were also significantly higher than those for the systems with undoped DNPs. Another way to compare the electrochemical behavior is via the current density values at a given potential, e.g., 0.4 V. Here, a value of 80 μA cm^{-2} Pt was observed with Pt/DNP, and 1600 μA cm^{-2} Pt for Pt–Ru/DNP. For Pt/BDDNP, a value of 350 μA cm^{-2} Pt was obtained and for Pt–Ru/BDDNP a value of 3900 μA cm^{-2} Pt. A third way is to compare the methanol oxidation onset potential. These values were 0.21, 0.18, 0.25, and 0.10 V for Pt/DNP, Pt–Ru/DNP, Pt/BDDNP, and Pt–Ru/BDDNP, respectively, indicating the highest activity for the latter.

Chemically reduced samples prepared using SDBS were also tested in an electrochemical cell containing 1 M methanol solution in 0.5 M H_2SO_4. Figure 8a shows a comparison between cyclic voltammograms for Pt/DNPs and Pt–Ru/DNPs in the potential range from 0.8 to −0.2 V (initial potential, 0.0 V). The Pt–Ru/DNPs catalytic system showed a lower value (130 μA cm^{-2}Pt) than that for Pt/DNPs (180 μA cm^{-2}Pt). Figure 8b shows a comparison between cyclic voltammograms for Pt/BDDNPs and Pt–Ru/BDDNPs in the potential range from 0.8 to −0.2 V (initial potential 0.0 V). It can be seen that the current densities were higher for the Pt/BDDNPs catalytic system (430 μA cm^{-2} Pt) than that for Pt–Ru/BDDNPs (310 μA cm^{-2} Pt). The current density values observed at 0.4 V also exhibited behavior similar to that shown in Figure 7. A value of 40 μA cm^{-2} Pt was observed with Pt/DNP, and 90 μA cm^{-2} Pt for Pt–Ru/DNP. For Pt/BDDNP, a value of 25 μA cm^{-2} Pt was obtained and for Pt–Ru/BDDNP a value of 150 μA cm^{-2} Pt. The methanol oxidation onset potentials were 0.45, 0.29, 0.30, and 0.18 V for Pt/DNP, Pt–Ru/DNP, Pt/BDDNP, and Pt–Ru/BDDNP, respectively, again showing the highest activity for the latter.

2.5.7. Anodic Characterization and Polarization Measurements (25, 60, 80 °C). The fabricated MEAs were characterized by SEM to observe the homogeneity and determine the thicknesses of the catalyst layers. Figure 9 shows a SEM micrograph of a MEA corresponding to

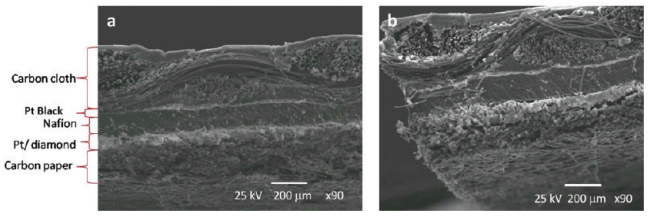

Figure 9. SEM micrographs of MEA made with platinum nanoparticles supported on undoped diamond nanoparticles: (a) middle area of the MEA, and (b) edge of the MEA.

platinum nanoparticles supported on undoped diamond nanoparticles (sample 1 in Table 1). All eight samples were characterized; they showed good homogeneity in the anode and cathode catalyst thicknesses. Anode catalyst layers exhibited thicknesses between 60 and 70 μm, and the cathode catalyst layers were between 10 and 15 μm.

Figures 10 and 11 show the potential − current density curves for the various catalysts: Pt/undoped DNPs, Pt–Ru/undoped DNPs, Pt/BDDNPs and Pt–Ru/BDDNPs, prepared without surfactant, and those synthesized using the surfactant; these demonstrated a strong effect of temperature for all samples. Figure 10 corresponds to those obtained with the catalyst samples that were prepared using excess reducing agent and high platinum loading (samples 1, 2, 3, and 4 of Table 1). Figure 11 corresponds to those catalysts prepared by using excess reducing agent, an excess of SDBS, and high platinum loading (samples 5, 6, 7, and 8 of Table 1).

As seen, the current densities increased according to different parameters such as platinum and ruthenium loadings, type of catalyst support (DNPs or BDDNPs), and temperature. In general, lower current densities were observed for Pt/DNP and Pt/BDDNP compared to those produced by Pt–Ru/DNP and Pt/BDDNP. When ruthenium was present, there was an increment in the current density for samples obtained using excess $NaBH_4$ agent, but this was not the case for samples obtained by the combination of both reducing agent and surfactant. The most efficient catalytic system was Pt/BDDNP obtained with a combination of reducing agent and surfactant.

The type of catalytic support material was also another parameter that influenced the current density responses. As observed in Figures 10 and 11, Pt/BDDNP and Pt–Ru/BDDNP, obtained using excess $NaBH_4$ or the combination of both reducing agent and surfactant, were the systems showing the highest current densities.

A significant temperature effect was evident in all cases; the catalytic systems showed an increment in current densities for the anode polarization as well as for the cell responses.

These results can be used to calculate the power produced by these catalytic systems in the fuel cell by multiplying together the current and voltage values for each catalytic system. These values are plotted versus the current density at 80 °C in Figure 12. The highest power was produced from catalytic systems where BDDNPs were used as the catalytic support.

3. DISCUSSION OF RESULTS

The electrochemical analysis of the various uncatalyzed materials (Figure 1a, b) shows interesting differences in capacitance among the bare glassy carbon (GC), Nafion film-covered GC, undoped DNP/GC, and BDDNP/GC electrodes. The lower capacitances for the DNP/GC and BDDNP/GC electrodes indicate indirectly that the diamond nanoparticles were effectively blocking the GC substrate and were thus only partially wetted. The degree of wetting is in fact difficult to determine and must differ between the two types of DNPs. For the BDDNP/GC, the fact that the particles are boron-doped, at least on the surface, should have led to a higher capacitance per unit wetted surface area, and therefore, the wetted surface area must have been smaller than that for the undoped particles. In any case, the low capacitance for the BDDNPs did not vary appreciably when a wider potential range was applied. The potential window for the BDDNP electrode was thus much larger than that for the undoped DNP/GC electrode, which is consistent with the lower degree of wetting but could also indicate that the film was either more effectively blocking the GC surface or was intrinsically of higher quality in terms of sp^2/sp^3 ratio. The wider potential range can be used to study a variety of electrochemical reactions on the BDDNP surface. There was also very little contribution from the redox couple centered at ca. 0.4 V vs Ag/AgCl, which was evident on all of the other electrodes and is often associated with the quinone/hydroquinone couple, observed for oxidized graphitic carbons. Thus, this sample appears to be largely free of such carbon. In

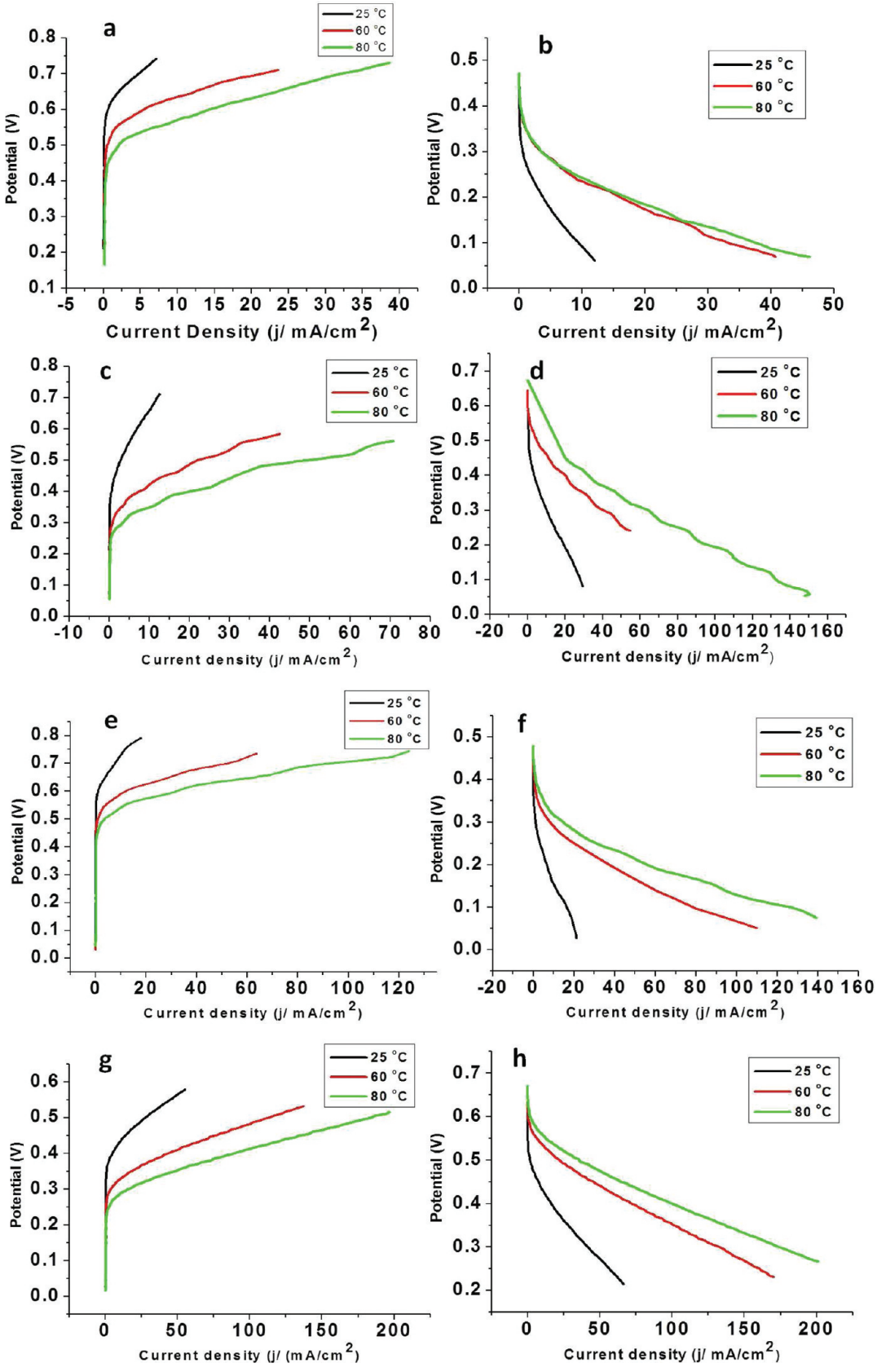

Figure 10. Voltage−current density curves for samples obtained by use of excess reducing agent and high platinum loading: (a, c, e, g) half-cell methanol oxidation polarization for Pt/DNPs, Pt−Ru/DNPs, Pt/BDDNPs, and Pt−Ru/BDDNPs respectively; (b, d, f, h) full-cell (methanol-air) polarization curves for anodes prepared with Pt/DNPs, Pt−Ru/DNPs, Pt/BDDNPs, and Pt−Ru/BDDNPs, respectively, corresponding to samples 1, 2, 3, and 4 of Table 1.

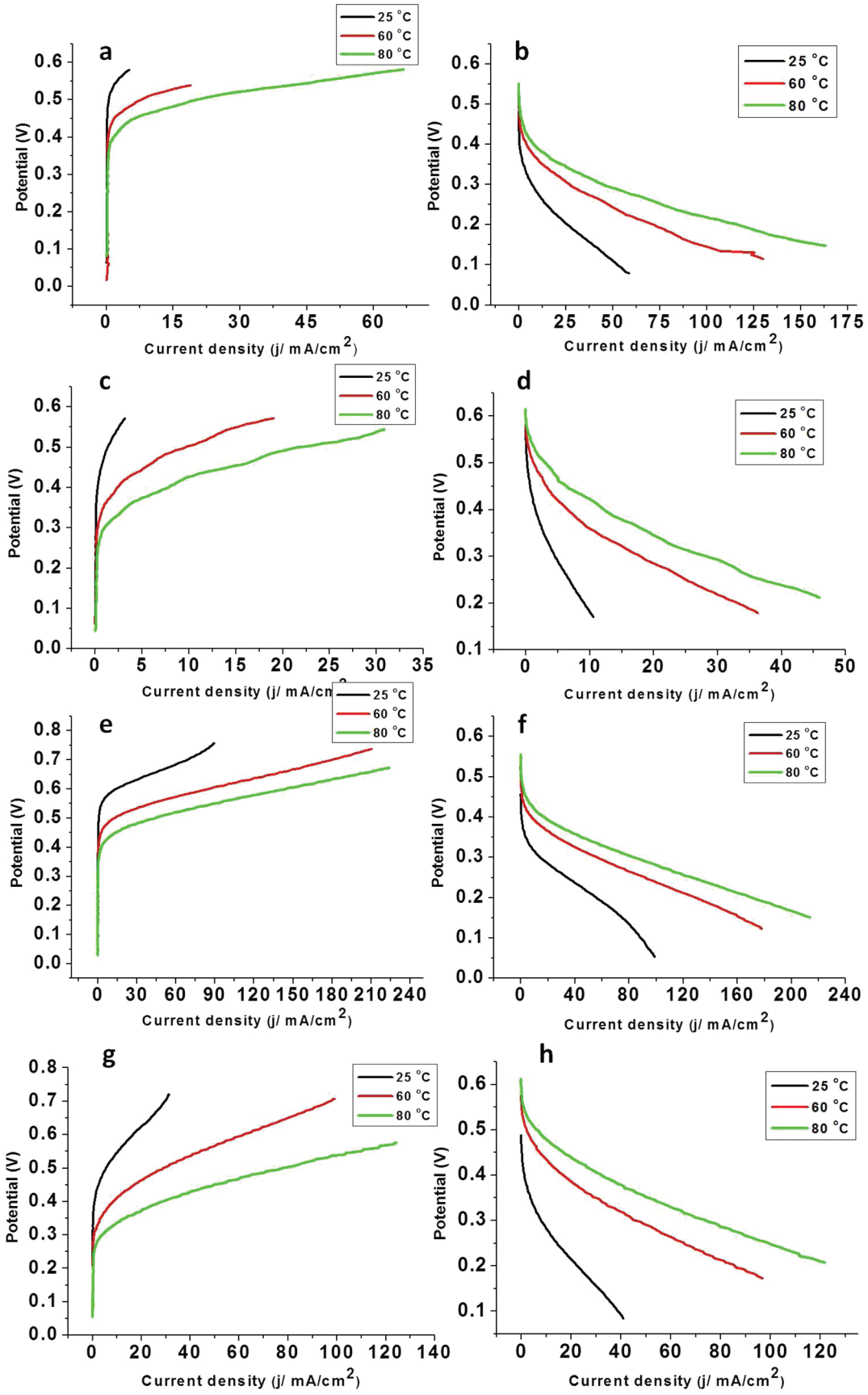

Figure 11. Current–voltage curves for samples obtained by use of excess reducing agent, SDBS, and high platinum loading: (a, c, e, g) half-cell methanol oxidation polarization for Pt/DNPs, Pt–Ru/DNPs, Pt/BDDNPs, and Pt–Ru/BDDNPs respectively; (b, d, f, h) full-cell (methanol-air) polarization curves for anodes prepared with Pt/DNPs, Pt–Ru/DNPs, Pt/BDDNPs, and Pt–Ru/BDDNPs, respectively, corresponding to samples 5, 6, 7, and 8 of Table 1.

dx.doi.org/10.1021/am2018628 | ACS Appl. Mater. Interfaces 2012, 4, 1134–1147

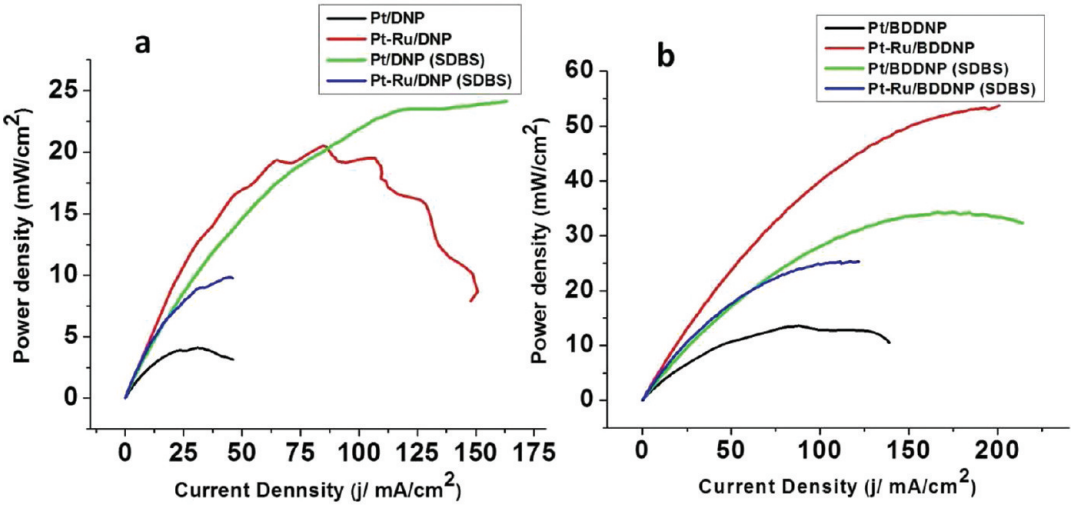

Figure 12. Power produced by direct methanol fuel cells at 80 °C with anodes prepared with: (a) undoped DNPs decorated with Pt (black) and Pt–Ru (red) catalysts synthesized by use of excess $NaBH_4$, and Pt (green) and Pt–Ru (blue) synthesized by use of excess $NaBH_4$ with SDBS; (b) BDDNPs decorated with Pt (black) and Pt–Ru (red) catalysts synthesized by using excess $NaBH_4$, and Pt (green) and Pt–Ru (blue) synthesized by use of excess $NaBH_4$ with SDBS.

terms of electrocatalyst support applications, the major conclusion based on these results is that the BDDNPs are expected to be highly electrochemically stable, particularly at higher potentials, because of the absence of cyclic voltammetric features due to graphitic carbon, which is known to be vulnerable to electrochemical oxidation.

The X-ray diffraction analyses showed differences among the samples containing Pt and Pt–Ru catalysts. Samples with higher percentages of platinum and less ruthenium prepared using excess reducing agent showed very different intensities in the XRD patterns (see the Supporting Information). The diamond (111) and (220) peaks were of low intensity on undoped DNPs; however, in the BDDNP patterns, these peaks were barely distinguishable. When ruthenium was present, the Pt (111) peaks showed much lower intensity and had larger full widths at half-maximum (FWHM) than those for pure Pt (111) on undoped DNPs and BDDNPs. Other Pt peaks were also much lower when ruthenium was present, which indicates that ruthenium atoms were introducing some disorder into the platinum crystal structure. XRD results of samples obtained with excess reducing agent and surfactant are shown in the Supporting Information, showing the characteristic peaks of Pt and Pt–Ru catalysts.

In our previous work,[33] from XPS results, the atomic percentage of boron was determined for the BDDNP sample, giving a value of 0.68 at %; the boron distribution is unknown, because the XPS photoelectrons are detectable from depths of 10–100 nm, compared to the particle diameters in the 6–8 nm range. The C 1s signal in this sample shows carbonyl and carboxylic groups; however, in samples with Pt and Pt–Ru catalysts, the intensities of these peaks were lower than those on the clean BDDNPs, which may indicate that the metals interact with these carboxylic acid groups.

When using a high percentage of platinum and a reducing agent, the XPS spectra of undoped DNPs and BDDNPs with platinum and ruthenium showed clear evidence that these metals deposit on alcohol (–C–OH) and carboxylic acid (–COOH) groups on the diamond surface (see the Supporting Information), as observed from the C 1s high resolution spectra. In samples corresponding to undoped DNPs, and BDDNPs modified with platinum and ruthenium nanoparticles, metallic platinum, platinum oxides (Pt $4f_{7/2}$, 71–72 eV; Pt $4f_{5/2}$, 74–75 eV) and metallic ruthenium (3p region 462 eV), with a small signal from the water ligand (466 eV), were also present, showing well-defined peaks. Table 2 indicates the functional groups present on the carbon surface for samples 1 to 6 from Table 1, as well as the presence of Pt and Ru, indicated by their binding energies. In our previous work,[33] (as also shown in the Supporting Information) diffuse reflectance infrared Fourier transform spectral (DRIFTS) analyses of undoped DNPs showed that functional groups present on the undoped DNP surface exhibited lower intensity bands (ν-C=O, ν $-CH_2$, ν –C–O–C–, ν $-CO_2$) or disappeared (ν –OH and ν $-CH_3$) after the DNPs were deposited with metallic Pt nanoparticles, which indicates that platinum deposition takes place mainly on sites corresponding to –OH and $-CH_3$ groups.

As can be seen in TEM micrographs of samples containing DNPs decorated with metallic platinum and ruthenium nanoparticles (Figure 2a, b), the atomic planes of the nanocrystals can be clearly observed. The sizes of these metallic crystals were less than 5 nm, consistent with the values obtained from the XRD results. However, there was also some agglomeration of the nanoparticles. The Pt/BDDNP and Pt–Ru/BDDNP samples (Figure 2c, d) were also characterized by TEM; these showed the crystal facets corresponding to the BDDNPs, with sizes of ca. 6 nm, and Pt and Pt–Ru nanoparticles which were less than 5 nm. Here also, the atomic planes of the nanocrystals can be clearly observed. There was also some agglomeration, with the DNPs being almost totally covered due to the high percentage of metallic nanoparticles.

When high percentages of platinum and a surfactant were used, improved distributions of metallic platinum and ruthenium nanoparticles were observed (Figure 3a–d). However, some aggregation of nanoparticles could not be avoided. As observed in Figure 3d, the DNPs were almost totally covered with Pt–Ru/BDDNPs. The metal particle sizes were less than 4 nm. These samples also showed the crystal planes of the platinum and ruthenium nanoparticles. We can

say that these metallic nanoparticles are alloys of Pt−Ru, because the XRD spectra did not exhibit any peak characteristic of Ru alone.

To determine the ratios of metals present in the samples, they were characterized by the EDX technique, but unfortunately, it was not possible to analyze single nanoparticles. Results indicate that the observed proportions of platinum and ruthenium corresponded well to those used in the synthesis (see the Supporting Information).

Although the platinum active surface area can be determined in a straightforward manner,[44] that for a bimetallic catalyst such as Pt−Ru is more complex, because the current for desorption of hydrogen on platinum overlaps the anodic current for OH adsorption on the ruthenium surface, and it is problematic to draw a baseline to determine the area under the adsorption/desorption peaks. To overcome this problem, researchers often use CO oxidative desorption (CO stripping). The value of charge used in CO desorption calculations was 420 μC cm^{-2}.[44] Cyclic voltammograms of adsorption/desorption of hydrogen and CO desorption, corresponding to samples in which excess reducing agent was used, are shown in Figure 4a, b (inset) and, Figure 5a, b (inset) for Pt/DNP, Pt−Ru/DNP, Pt/BDDNP, and Pt−Ru/BDDNP, respectively. They showed characteristic peaks of hydrogen adsorption/desorption on the polycrystalline Pt surface, which was cleaned electrochemically by continuous cycles from −0.2 to 0.8 V for electrodes with Pt only and from −0.2 to 0.6 V for electrodes with Pt−Ru catalyst.[45] The voltammograms also showed hydroxide (PtOH) and oxide (PtO) formation at positive potentials. With pure Pt (Figures 4a, 5a, and 6a), hydrogen adsorption (as well as desorption) exhibited two main peaks, whereas when Ru was present (Figures 4b, 5b, and 6b), these peaks merged into a single peak, and the current also increased.

The values obtained for the Pt surface area were relatively low, compared with those reported in the literature using Vulcan carbon as a support (electrochemically active surface area for Pt:Ru, 80:20 at%: 582 cm^2 Pt mg^{-1}).[46] Furthermore, there was a slight increase in Pt surface area values (hydrogen adsorption/desorption) for samples obtained by using both reducing agent and surfactant, compared with those obtained with the reducing agent only (Figure 6a, b (inset) compared with Figure 5a, b).

Cyclic voltammograms (Figure 7) obtained for 1 M methanol in 0.5 M H_2SO_4 showed the current responses normalized by the Pt active surface area obtained for electrocatalysts prepared with reducing agent only. There was a large increase in current density (factor of ca. 10) and a potential shift to lower values when ruthenium was present, comparing Pt/DNP and Pt−Ru/DNP. This can be explained by the bifunctional mechanism, in which ruthenium promotes the generation of oxygen-containing species, aiding the oxidation of CO adsorbed on the Pt surface.[44] The same phenomena can be observed for the BDDNP-supported materials, i.e., the current density for PtRu/BDDNP was approximately ten times higher than that for Pt/BDDNP. Furthermore, the difference between the DNP support and BDDNP support was striking: the current density for Pt−Ru/BDDNP was approximately four times higher than that for Pt−Ru/DNP; this suggests that the improved electronic conductivity for the doped material may have been playing an important role, e.g., in making better contact between DNPs or better contact between metal and DNPs. The current density values observed at 0.4 V, and the onset potentials also provide a useful indicator of the activity and indicate the strong effects of Ru alloying and boron doping. These values are consistent with the high catalytic activity of the Pt−Ru/BDDNP system.

It was expected that the peak current densities for methanol oxidation should have increased even further due to improved dispersion of the metal catalysts on the undoped DNPs and BDDNPs as a result of excess of surfactant. Figures 8a,b show cyclic voltammograms obtained for 1 M methanol in 0.5 M H_2SO_4 for materials that were prepared using both excess reductant and surfactant. However, the Pt−Ru/DNP and Pt−Ru/BDDNP electrodes did not behave as expected; they showed lower peak current densities than those for the Pt/DNP and Pt/BDDNP electrodes. Nevertheless, the current density values observed at 0.4 V (positive-going sweep) did show an enhancement when ruthenium was present for both DNPs as well as BDDNPs. The current density values were lower than those obtained by using excess $NaBH_4$ without adding SDBS. This may have been due to either a poorer dispersion or possibly residual surfactant acting as blocking agent. However, the tendency of improvement with the addition of ruthenium, and also by changing the catalyst support, was maintained and was similar to those for the systems obtained using excess $NaBH_4$ without SDBS. Considering the onset potentials, it is clear that the Pt−Ru/BDDNP system is the most active. Furthermore, the current densities for Pt/BDDNP and Pt−Ru/BDDNP at 0.4 V were higher than those for Pt/DNP and Pt−Ru/DNP. This result still supports the idea that the doping and associated enhanced conductivity lead to improved performance.

The beneficial effect of the BDDNP support, compared to the undoped one, may be ascribed to the improved electronic conductivity. Nevertheless, one may note that when the electrocatalyst is deposited in the absence of SDBS the use of the boron-doped substrate results in an increase of the current density at 0.4 V from 80 to 350 uA cm^{-2} (ca. 4.4 times) for Pt, while for PtRu the increase is less important (ca. 2.4 times) i.e., from 1600 to 3900 uA cm^{-2}. On the other hand, for samples prepared using SDBS, the effect of the boron-doped substrate is less marked for PtRu (the current density at 0.4 V increases from 90 to 150 uA cm^{-2}), and even opposite for Pt (the current density decreases from 40 to 25 uA-cm^{-2}). It may be possible that the boron-doped substrate enhances CO oxidative desorption compared to undoped diamond. Nevertheless, a more detailed analysis needs to be done before reaching a definite conclusion on the boron doping effect on CO oxidation.

The brush painting is also an important step, because the homogeneity of the catalyst layers also affects the voltage losses in the cell and consequently the power produced. As is seen in the SEM micrographs (Figure 9), homogeneous anode and cathode layers were obtained by painting and drying the GDL. The thicknesses of the catalyst layers were uniform across the entire electrode (compare Figure 9, parts a and b). Metal loadings were also near the desired value (4 mg cm^{-2}).

For the types of MEAs shown in Figure 9, current−voltage curves were obtained by polarization of the anodes (versus a hydrogen-fed cathode) corresponding to the catalytic systems (1, 2, 3, 4 in Table 1), and are shown in Figure 10a, c, e, g; the curves showed increasing current densities at given voltages, first, when only Pt (a) was present, followed by the addition of Ru (Pt−Ru bimetallic catalyst) (c); and when the catalyst support was BDDNP (Figure 10e, g); these results again confirm that the presence of Ru and BDDNP contribute to

performance. A temperature effect was also observed; i.e., higher current densities at higher temperatures.

In the case of the cell actually operating in a power generation mode (methanol fed through the anode and air through the cathode), similar trends were observed (Figure 10b, d, f, h), where it can be seen that the open circuit voltages of the catalytic systems containing Pt−Ru on DNPs (d) and BDDNPs (h) were ca. 0.7 V, which indicates that approximately 20−30% efficiency could be obtained from the fuel cell as an upper limit. For comparison, if hydrogen is used as a fuel, the efficiency is typically around 50% at high temperatures.[47] In contrast, for the catalysts containing only Pt, the initial potential was around 0.5 V, indicating lower efficiency. It can be also observed in the current−voltage curves (Figure 10b, d, f, h), that the voltage decreased rapidly in the low current density (activation) region, particularly at room temperature; at all temperatures, the curves exhibited linear behavior, i.e., ohmic polarization. In the highest current density region of the curves, there was no indication of losses due to concentration polarization, i.e., no rapid drop in voltage.

Anode polarization current−voltage curves for catalyst systems 5, 6, 7, 8 in Table 1 (both reductant and surfactant), shown in Figure 11a, c, e, g show the relatively high voltages required when only Pt (a) was present and the decreases in voltage obtained for the Pt−Ru (c) bimetallic catalyst; and that obtained when the Pt support was BDDNP (e), showing the beneficial effects of these factors. However, Figure 11 g (Pt−Ru/BDDNP) shows generally higher voltages than expected at 25 and 60 °C, because this system has the best catalyst, better support, and better dispersion. Nevertheless, at 80 °C the voltages were indeed the lowest, showing that this catalyst was able to operate well at this temperature. Furthermore, the current density values for this catalytic system were higher than those for the system synthesized using excess $NaBH_4$ and with the DNP support.

In the case of full cell performance, similar trends were observed (Figure 11b, d, f, h), where it can be seen that the open circuit voltages of these catalytic systems were ca. 0.65 V, which indicates that approximately 20−30% efficiency could be obtained from the fuel cell as an upper limit. However, the low current (activation) process was still influential in limiting the cell performance. Losses in cell voltage were generally smaller than those for the four first catalytic systems, indicating the benefit of the better catalyst dispersion.

As shown in panels a and b in Figure 12, the power densities in mW cm^{-2} produced by all systems at 80 °C, are compared for the DNP and BDDNP support materials, demonstrating that the latter performed better; in particular, the Pt−Ru/BDDNP catalytic system (Figure 12 b) exhibited superior power density, with no decay observed in the range shown, in contrast to the other systems. Higher power densities were produced by the catalytic systems using BDDNPs, by a factor of approximately two, compared to those for the catalytic systems using undoped DNPs as the support.

4. CONCLUSIONS

The route used to prepare the suspensions (inks) of DNPs and BDDNPs for the electrochemical studies was shown to be well-suited to obtain useful electrochemical information on these nanoparticle diamond supported systems. The cyclic voltammetry results showed that there were significant differences between the undoped DNP and BDDNPs samples, with the latter exhibiting superior characteristics in terms of various electrochemical applications, including that of catalyst support. For the latter application, perhaps the most important consequence of the observed low capacitance and wide potential window might be the expected stability, particularly at higher potentials.

Chemical reduction of metal nanoparticles at the nanometer scale was successfully performed using DNPs and BDDNPs as support materials by using an excess of a mild reducing agent ($NaBH_4$) and a surfactant (SDBS). X-ray diffraction peaks for the metallic nanoparticles were clearly observed. The XPS and DRIFTS results provided important information about the type of surface functional groups on the diamond involved in the metal deposition. These techniques indicated that platinum ions interact, become reduced, and are deposited as metal on sites containing mainly −OH and CH_2 (or $-CH_3$) groups. This analysis should be verified by using a more sensitive technique such as far-infrared spectroscopy in order to determine the interaction between platinum and oxygen species.

TEM micrographs showed that the nanosize metals were crystals of less than 5 nm, which exhibited lattice fringes for the atomic planes of metal material, indicating good crystallinity, as well as of those of diamond. The distribution and dispersion of diamond and reduced metal nanoparticles were also clearly observed. Enhanced dispersion of some samples obtained through the use of SDBS surfactant was also observed.

Homogeneous layers of catalyst systems on GDLs were obtained by the brush painting technique. This process was reproducible, as evidenced by the similarity of thicknesses of the layers prepared for anodes and cathodes, as determined by SEM. Metal loadings were close to the expected values. Drying and weighing steps were also important, as well as the humidity control at the conclusion of the painting process. Anodic polarization results for methanol oxidation demonstrated that respectable current densities, in the range of mA cm^{-2}, could be obtained with both undoped DNPs and BDDNPs decorated with Pt and Pt−Ru catalysts prepared using excess reducing agent and surfactant.

The power densities obtained from the best catalytic system (ca. 55 mW cm^{-2} for Pt−Ru/BDDNP) were comparable to those obtained with amorphous carbon-supported catalytic systems, which are typically around 60 and 70 mW cm^{-2} at the same temperature.[48] On the basis of the single fuel cell testing, it can be concluded that undoped DNPs and BDDNPs can be used as practical electrocatalyst supports for Pt and Pt−Ru in direct methanol fuel cells or hydrogen-fueled polymer electrolyte fuel cells.

■ ASSOCIATED CONTENT

Supporting Information

Cyclic voltammograms, FT-IR, X-ray fluorescence, and X-ray diffraction data of purified DNPs, DNPs reacted with the reducing agent $NaBH_4$, Pt/undoped DNPs, Pt−Ru/undoped DNPs, Pt/boron doped DNPs, and Pt−Ru/boron doped DNPs catalysts. This material is available free of charge via the Internet at http://pubs.acs.org/.

■ AUTHOR INFORMATION

Corresponding Author

*E-mail: carlos.cabrera2@upr.edu; 787-764-0000-1-4807.

Notes

The authors declare no competing financial interest.

■ ACKNOWLEDGMENTS

This work was supported by the NSF Center for Hierarchical Manufacturing at the University of Massachusetts Grant CMMI-0531171, NASA-URC Center for Advanced Nanoscale Materials Grant NNX10AQ17A, and NSF-EPSCoR Institute for Functional Nanomaterials Grants OIA-0701525 and EPS-1002410. The authors acknowledge The Cornell Center for Materials Research (CCMR) for the TEM Analyses. The CCMR is funded by the National Science Foundation as part of the Materials Research Science and Engineering Centers program under Award Number DMR-0520404.

■ REFERENCES

(1) Viswanathan, B.; Scibioh, M. A. *Fuel Cells: Principles and Applications*; Taylor & Francis: New York, 2008
(2) Takasu, Y.; Kawaguchi, T.; Sugimoto, W.; Murakami, Y. *Electrochim. Acta* **2003**, *48*, 3861.
(3) Gloaguen, F.; Leger, J. M.; Lamy, C. *J. Appl. Electrochem.* **1997**, *27*, 1052.
(4) Rao, V.; Simonov, P. A.; Savinova, E. R.; Plaksin, G. V.; Cherepanova, S. V.; Kryukova, G. N.; Stimming, U. *J. Power Sources* **2005**, *145*, 178.
(5) Antolini, E. *Appl. Catal., B* **2009**, *88*, 1.
(6) Porcard, N. L.; Alsmeyer, D. C.; McCreery, R. L.; Neenan, T. X.; Callstrom, M. R. *J. Am. Chem. Soc.* **1992**, *114*, 769.
(7) Mani, R. C.; Sharma, S.; Sunkara, M. K.; Gullapalli, J.; Baldwin, R. P.; Rao, R.; Rao, A. M.; Cowley, J. M. *Electrochem. Solid-State Lett.* **2002**, *5*, E32.
(8) Fischer, A. E.; Swain, G. M. *J. Electrochem. Soc.* **2005**, *152*, B369.
(9) Hayashi, Y.; Mori, D.; Soga, T.; Jimbo, T. *Phys. Solid State* **2004**, *46*, 733.
(10) Danilenko, V. *Phys. Solid State* **2004**, *46*, 595.
(11) Pleskov, Y. V. *Russ. J.Electrochem.* **2002**, *38*, 1275.
(12) Bogatyreva, G.; Marinich, M.; Ishchenko, E.; Gvyazdovskaya, V.; Bazalii, G.; Oleinik, N. *Phys. Solid State* **2004**, *46*, 738.
(13) Osswald, S.; Yushin, G.; Mochalin, V.; Kucheyev, S. O.; Gogotsi, Y. *J. Am. Chem. Soc.* **2006**, *128*, 11635.
(14) Rinzler, A. G.; Liu, J.; Dai, H.; Nikolaev, P.; Huffman, C. B.; Rodriguez-Macias, F. J.; Boul, P. J.; Lu, A. H.; Heymann, D.; Colbert, D. T.; Lee, R. S.; Fischer, J. E.; Rao, A. M.; Eklund, P. C.; Smalley, R. E. *Appl. Phys. A: Mater. Sci. Proc.* **1998**, *67*, 29.
(15) La - Torre - Riveros, L., Tryk, D. A.; Cabrera, C. R. *Rev. Adv. Mater. Sci.*, **2005**, *10*, 256.
(16) Holt, K. B.; Caruana, D. J.; Millán-Barrios, E. J. *J. Am. Chem. Soc.* **2009**, *131*, 11272.
(17) Holt, K. B. *Phys. Chem. Chem. Phys.* **2010**, *12*, 2048.
(18) Conrad, J. R.; Radtke, J. L.; Dodd, R. A.; Worzala, F. J.; Tran, N. C. *J. Appl. Phys.* **1987**, *62*, 4591.
(19) Suarez, A.; Prelas, M. A.; Ghosh, T. K.; Tompson, R. V.; Loyalka, S. K.; Miller, W. H.; Viswanath, D. S. *J. Wide Bandgap Mater.* **2002**, *10*, 15.
(20) Mendez, A. E.; Prelas, M. A.; Glascock, M.; Ghosh, T. K. *Mater. Res. Soc. Symp. Proc.* **2006**, *929*, 0929-II05−03.
(21) Jeon, M. K.; Won, J. Y.; Lee, K. R.; Woo, S. I. *Electrochem. Commun.* **2007**, *9*, 2163.
(22) Aricò, A. S.; Poltarzewski, Z.; Kim, H.; Morana, A.; Giordano, N.; Antonucci, V. *J. Power Sources* **1995**, *55*, 159.
(23) Zhang, X.; Chan, K. Y. *Chem. Mater.* **2002**, *15* (2), 451−459.
(24) Liu, Z.; Lee, J. Y.; Han, M.; Chen, W.; Gan, L. M. *J. Mater. Chem.* **2002**, *12*, 2453.
(25) Watanabe, M.; Uchida, M.; Motoo, S. *J. Electroanal. Chem. Interfacial Electrochem.* **1987**, *229*, 395.
(26) Paulus, U. A.; Endruschat, U.; Feldmeyer, G. J.; Schmidt, T. J.; Bönnemann, H.; Behm, R. J. *J. Catal.* **2000**, *195*, 383.
(27) Aricò, A. S.; Baglio, V.; Di Blasi, A.; Modica, E.; Antonucci, P. L.; Antonucci, V. *J. Electroanal. Chem.* **2003**, *557*, 167.
(28) Xu, W.; Zhou, X.; Liu, C.; Xing, W.; Lu, T. *Electrochem. Commun.* **2007**, *9*, 1002.
(29) Fu, X.; Yu, H.; Peng, F.; Wang, H.; Qian, Y. *Appl. Cat. A: General* **2007**, *321*, 190.
(30) Nersisyan, H. H.; Lee, J. H.; Son, H. T.; Won, C. W.; Maeng, D. Y. *Mater. Res. Bull.* **2003**, *38*, 949.
(31) Im, D. H.; Park, S. Y.; Hyun, S. H.; Lee, B. Y.; Kim, Y. H. *J. Mater. Sci.* **2004**, *39*, 3629.
(32) Il Gyo, K.; Myoung Seok, L.; Jae Hee, S.; Jae Hwan, A.; Woong Moo, L. *J. Mater. Chem* **2005**, *15*, 4125.
(33) La-Torre-Riveros, L.; Abel-Tatis, E.; Méndez-Torres, A. E.; Tryk, D. A.; Prelas, M.; Cabrera, C. R. *J. Nanopart. Res.* **2011**, *13*, 2997.
(34) Cindrella, L.; Kannan, A. M.; Lin, J. F.; Saminathan, K.; Ho, Y.; Lin, C. W.; Wertz, J. *J. Power Sources* **2009**, *194*, 146.
(35) Iwasita, T.; Hoster, H.; John-Anacker, A.; Lin, W. F.; Vielstich, W. *Langmuir* **2000**, *16*, 522.
(36) Liu, R.; Smotkin, E. S. *J. Electroanal. Chem.* **2002**, *535*, 49.
(37) Beden, B.; Kadirgan, F.; Lamy, C.; Leger, J. M. *J. Electroanal. Chem.* **1981**, *127*, 75.
(38) La-Torre-Riveros, L.; Soto, K.; Scibioh, M. A.; Cabrera, C. R. *J. Electrochem. Soc.* **2010**, *157*, B831.
(39) Nakao, Y.; Kaeriyama, K. *J. Colloid Interface Sci.* **1986**, *110*, 82.
(40) *Membrane Electrode Assembly (MEA) Preparation and Evaluation*; Technology and Education Center for Renewable Energy, Inter-American University of Puerto Rico: Bayamon, Puerto Rico, 2009.
(41) Lobato, J.; Rodrigo, M. A.; Linares, J. J.; Scott, K. *J. Power Sources* **2006**, *157*, 284.
(42) Diaz-Morales, R. R.; Liu, R.; Fachini, E.; Chen, G.; Segre, C. U.; Martinez, A.; Cabrera, C.; Smotkin, E. S. *J. Electrochem. Soc.* **2004**, *151* (9), A1314−A1318.
(43) National institute of standards and technology, nist.gov, 2010.
(44) Vidakovic, T.; Christov, M.; Sundmacher, K. *Electrochim. Acta* **2007**, *52*, 5606.
(45) Herrero, E.; Franaszczuk, K.; Wieckowski, A. *J. Phys. Chem.* **1994**, *98*, 5074.
(46) Hsieh, C. T.; Lin, J. Y.; Yang, S. Y. *Phys. E* **2009**, *41*, 373.
(47) Thomas, S. C.; Ren, X.; Gottesfeld, S.; Zelenay, P. *Electrochim. Acta* **2002**, *47*, 3741.
(48) Liang, Y.; Li, J.; Xu, Q.-C.; Hu, R.-Z.; Lin, J.-D.; Liao, D.-W. *J. Alloys Compd.* **2008**, *465*, 296.